

Quantitative nondiagonal phase field modeling of eutectic and eutectoid transformations

Kai Wang 

Institute for Energy and Climate Research, IEK-2, Forschungszentrum Jülich, D-52425 Jülich, Germany

Guillaume Boussinot

Access e.V., Intzestr. 5, D-52072 Aachen, Germany

Efim A. Brener 

*Institute for Energy and Climate Research, IEK-2, Forschungszentrum Jülich, D-52425 Jülich, Germany
and Peter Grünberg Institut, Forschungszentrum Jülich, D-52425 Jülich, Germany*

Robert Spatschek 

*Institute for Energy and Climate Research, IEK-2, Forschungszentrum Jülich, D-52425 Jülich, Germany
and JARA-ENERGY, 52425 Jülich, Germany*



(Received 24 February 2021; revised 6 May 2021; accepted 6 May 2021; published 26 May 2021)

We develop a three-phase field model for the simulation of eutectic and eutectoid transformations on the basis of a nondiagonal model obeying Onsager relations for a kinetic cross coupling between diffusion and the phase fields. This model overcomes the limitations of existing phase field models concerning the fulfillment of local equilibrium boundary conditions at the transformation fronts in the case of a finite diffusional contrast between the phases. We benchmark our model in the well understood one-sided case with diffusion only in the parent phase against results from the literature. In addition to this solidification scenario, the case of solid-state transformations with diffusion in the growing phases is investigated. Our simulations validate the relevance of the theory developed by Ankit *et al.* [*Acta Mater.* **61**, 4245 (2013)], that describes in a single frame the two limiting regimes where diffusion mainly takes place whether in the mother phase or in the growing phases. In both the one-sided and two-sided cases, we verify the necessity of the kinetic cross coupling for quantitative phase field simulations.

DOI: [10.1103/PhysRevB.103.184111](https://doi.org/10.1103/PhysRevB.103.184111)

I. INTRODUCTION

Eutectic and eutectoid alloys are widely used as structural materials due to their excellent mechanical properties [1,2]. During eutectic and eutectoid transformations two solid phases (α and β) emerge from the parent phase (γ). The prediction of their growth kinetics is the prerequisite to forecast the complex growth patterns. In addition to the inherent materials properties, such as interfacial energies, diffusivities, and the nature of phase diagrams, solidification conditions such as the undercooling for isothermal transformations, the magnitude and orientation of the temperature gradient for directional solidification, as well as additional impurities influence the growth kinetics.

Lamellar microstructures are common growth patterns during eutectic and eutectoid transformations. For the lamellar growth in a binary alloy during eutectic solidification, Jackson and Hunt (JH) have adopted the Zener-Hillert model [3,4] and found a steady-state solution which gives an analytical expression of the average undercooling of the solidification front ΔT , depending on the growth velocity V and the lamellar spacing λ [5],

$$\Delta T = K_1^{\text{JH}} \lambda V + \frac{K_2^{\text{JH}}}{\lambda}, \quad (1)$$

where K_1^{JH} and K_2^{JH} are constants that depend on the thermophysical properties of liquid and solid phases. The Jackson-Hunt theory assumes that the bulk diffusion takes place only in the mother phase γ (one-sided case), i.e., the diffusion coefficients in the growing α and β phases obey $D_\alpha, D_\beta \ll D_\gamma$. Although this hypothesis is reasonable for eutectic solidification for which the mother phase is the liquid phase, diffusion in the growing phases can play a crucial role during eutectoid transformations. In such a case, the mother phase is also a solid phase and the diffusivities in the growing phases are of the same order (two-sided case) or several orders of magnitudes larger than in the mother phase. For the pearlite transformation, which is a well-known eutectoid transformation, the diffusivity of ferrite is two orders of magnitudes larger than the one of austenite. The analytic velocity of the stable cooperative pearlite growth with diffusion restricted to austenite is much smaller than the experimental data [3,4]. Further studies of the pearlite transformation in the two-sided case were conducted by Ankit *et al.* [6]. They extended the Jackson-Hunt theory and obtained a linear relation to predict the pearlite growth velocity,

$$V = \frac{(\Delta T - \frac{K_2^{\text{JH}}}{\lambda})}{K_1^{\text{JH}} \lambda} \rho = V_{\text{JH}} \rho, \quad (2)$$

with

$$\rho = 1 + t_\alpha \mu_\alpha \eta_\alpha + t_\beta \mu_\beta \eta_\beta, \quad (3)$$

where $\mu_\alpha = D_\alpha/D_\gamma$ and $\mu_\beta = D_\beta/D_\gamma$. η_α and η_β are the equilibrium volume fractions of phases α and β , respectively. t_α and t_β are constants depending on the ratio of the liquidus slopes to the solidus slopes of α and β phases.

The phase field (PF) method has emerged in the last decades as an efficient way to investigate interface dynamics during eutectic and eutectoid transformations [7–11]. The characteristic feature of this diffuse interface approach is to avoid tracking an explicit moving interface by introducing a PF variable ϕ , which exhibits spatial variations inside the interface on the scale of the interface thickness W . The interface thickness has no physical meaning but is typically chosen to be orders of magnitude larger than the atomistic scale to simulate mesoscopic microstructure evolutions. This enhancement of the interface thickness gives rise to anomalous interface effects.

The elimination of these abnormal interface effects has been of particular interest in the past 20 years. In Ref. [12], this problem was solved, for equal diffusivity in the solid and liquid phase (symmetric model), by linking the classical PF model and the free-boundary problem based on the so-called thin-interface limit. This pioneering work made it possible to remove the abnormal interface effects and achieve local equilibrium boundary conditions by choosing the appropriate PF kinetic parameters. This quantitative PF model was extended to binary alloys with negligible solid diffusivity during solidification (one-sided model) [13]. A correction term called antitrapping current that is proportional to the interface velocity was introduced to remove the interface effects originating from the discontinuity of the chemical potential at the interface. However, for general alloy solidification with unequal diffusivities in the solid and parent phase (two-sided model), the thin-interface analysis of the classical PF model may not be achieved without altering the thermodynamics of the interface with some unphysical adsorption [14]. Only recently, a cross coupling between the conserved and nonconserved variables was introduced in the PF kinetic equations, in accordance with Onsager out-of-equilibrium thermodynamics. This yields a nondiagonal PF model with a new degree of freedom allowing to eliminate all the abnormal interface effects [15–18]. In Ref. [19], the capabilities of the nondiagonal PF model were investigated during the two-dimensional dendritic solidification of pure substances with diffusional contrast in the solid and liquid phases (two-sided) and benchmarked against Green’s function calculations and the Barbieri-Langer theory. The excellent agreement between the nondiagonal PF results and the sharp interface method calculations illustrates the requirement of the kinetic cross coupling and elimination of surface diffusion.

However, quantitatively modeling eutectic and eutectoid transformations is still a challenge for PF simulations, especially when the diffusivities in the parent and growing phases are arbitrary. For the one-sided case, Folch and Plapp [11] developed a quantitative PF model with antitrapping current to reproduce the free-boundary conditions. The advantage of this model is to ensure the disappearance of spurious third phases in the two-phase interface by proposing a fifth-order interpo-

lation function and linking the PF model to free-boundary descriptions. For the two-sided case, Ohno and Matsuura [20,21] extended the antitrapping current by an additional prefactor $(1 - D_s/D_l)$ for three-phase solidification.

The purpose of this paper is to extend the nondiagonal PF model for eutectic and eutectoid transformations in binary A-B alloys when the diffusivities in the growing phases are neither equal to the one in the mother phase nor negligible, to benchmark the quantitative capabilities of the extended nondiagonal PF model, and to better understand the role and effect of diffusion in the growing phases. Therefore, we first introduce the formulation of a nondiagonal three-phase field model. Subsequently, we present the elimination of the abnormal effects at the α/γ , β/γ , and α/β interfaces and the link to equilibrium boundary conditions. Following this, nondiagonal PF simulations are performed in the one-sided case to compare with boundary integral method calculations and Jackson-Hunt theory for a model alloy that is directionally solidified. Additionally, in the two-sided case, isothermal transformations at eutectoid and off-eutectoid compositions are carried out and the growth velocities at a steady state are compared to the extended Jackson-Hunt theory by Ankit *et al.* [6]. PF simulations without cross-coupling terms are also performed in order to evidence the necessity of using a nondiagonal PF model.

II. PHASE FIELD MODEL

In this section, we present the nondiagonal three-phase field model by defining three scalar phase field order parameters ϕ_i ($i = \alpha, \beta, \gamma$), to distinguish the different phases α , β , and γ , obeying the constraint

$$\sum_{i=\alpha,\beta,\gamma} \phi_i = 1. \quad (4)$$

In the following we use the vector notation $\vec{\phi} = (\phi_\alpha, \phi_\beta, \phi_\gamma)$. Generally, the phase field parameter ϕ_i represents the volume fraction of phase i and is allowed to vary from 0 to 1, such that $\phi_\alpha = 1, \phi_\beta = \phi_\gamma = 0$ indicates the α phase. Additionally, an α/β interface is characterized by a spatial profile of phase fields in which ϕ_α and ϕ_β smoothly vary from 0 to 1 across the diffusional interface.

A. Free-energy functional

We start with the Ginzburg-Landau-type free-energy functional,

$$F = \int_V dV \left[H \left\{ \frac{W^2}{2} \sum_{i=\alpha,\beta,\gamma} (\nabla \phi_i)^2 + \sum_{i=\alpha,\beta,\gamma} \phi_i^2 (1 - \phi_i)^2 \right\} + X f_c(\vec{\phi}, c, T) \right], \quad (5)$$

which consists of three parts. The first one represents the gradient energy term, in which W is the interface width. The second part is a triple-well potential, which is constructed as the sum of double-well potentials for all phase fields. The free-energy density H determines the height of the potential. The last term, formed as a function of phase fields $\vec{\phi}$, solute concentration c , and temperature T , describes the free energy

of the different bulk phases,

$$f_c(\vec{\phi}, c, T) = \frac{1}{2} \left[c - \sum_{i=\alpha, \beta, \gamma} A_i(T) g_i(\vec{\phi}) \right]^2 + \sum_{i=\alpha, \beta, \gamma} B_i(T) g_i(\vec{\phi}), \quad (6)$$

where $A_i(T)$ and $B_i(T)$ are functions of temperature T , to construct the desirable phase diagram, and g_i is an interpolating function, which is written as

$$g_i(\vec{\phi}) = \frac{\phi_i^2}{4} \{ 15(1 - \phi_i)[1 + \phi_i - (\phi_k - \phi_j)^2] + \phi_i(9\phi_i^2 - 5) \}, \quad (7)$$

where i, j, k are pairwise distinct (i.e., are all different). For binary interfaces, for example, for an α/β interface with $\vec{\phi} = (\phi, 1 - \phi, 0)$, the function $g_\alpha(\vec{\phi})$ reduces to the polynomial $p(\phi) = \phi^3(10 - 15\phi + 6\phi^2)$. The last term in Eq. (5) is parametrized by another free-energy density X that sets the relation between the capillary length and the interface width W through the ratio H/X (see later).

The chemical potential can be written as

$$u = \frac{\partial f_c}{\partial c} = c - \sum_{i=\alpha, \beta, \gamma} A_i(T) g_i(\vec{\phi}). \quad (8)$$

Specifically, the advantage of the fifth-order interpolation function employed in the chemical free-energy function is avoiding the appearance of spurious third-phase contributions in a two-phase interface [11].

B. Time evolution equations

We define our a scaled concentration field as

$$c = \frac{C - C_E}{C_\beta - C_\alpha}, \quad (9)$$

where C is the local alloy concentration, and C_E, C_α, C_β are the equilibrium concentrations at the eutectic and eutectoid temperature T_E of the parent phase (γ) and growing phases α and β , respectively. The concentration c is a conserved quantity that obeys the continuity equation

$$\dot{c} = -\nabla \cdot \mathbf{J}, \quad (10)$$

where \mathbf{J} is the diffusion flux.

Our goal is to write down a nondiagonal PF model in the spirit of Ref. [15] that formally maintains the symmetry between the different phase fields. In order to fulfill the condition (4), one may introduce a Lagrange multiplier in the free-energy functional and its elimination yields the following definitions:

$$\frac{\delta F}{\delta \phi_i} \Big|_{\sum \phi_n=1} = \frac{2}{3} \frac{\delta F}{\delta \phi_i} - \frac{1}{3} \frac{\delta F}{\delta \phi_j} - \frac{1}{3} \frac{\delta F}{\delta \phi_k}, \quad (11)$$

$$\nabla \phi_i \Big|_{\sum \phi_n=1} = \frac{2}{3} \nabla \phi_i - \frac{1}{3} \nabla \phi_j - \frac{1}{3} \nabla \phi_k. \quad (12)$$

Again, (i, j, k) is a permutation of (α, β, γ) . The terms on the left-hand side of these equations are operators explicitly

informing that the constraint in Eq. (4) is fulfilled, while on the right-hand side, the operators are calculated as if ϕ_α, ϕ_β , and ϕ_γ were independent. In particular, we have

$$\sum_i \frac{\delta F}{\delta \phi_i} \Big|_{\sum \phi_n=1} = 0, \quad (13)$$

$$\sum_i \nabla \phi_i \Big|_{\sum \phi_n=1} = 0. \quad (14)$$

The Onsager linear relations between the driving forces and the fluxes that define the kinetics within the PF model are then

$$-\frac{\delta F}{\delta \phi_i} \Big|_{\sum \phi_n=1} = \tau \dot{\phi}_i + \{ MW \nabla \phi_i \Big|_{\sum \phi_n=1} \} \cdot \mathbf{J}, \quad (15)$$

$$-\nabla \frac{\delta F}{\delta c} = -\nabla u = \sum_{i=\alpha, \beta, \gamma} \{ MW \nabla \phi_i \Big|_{\sum \phi_n=1} \} \dot{\phi}_i + \frac{\mathbf{J}}{D}, \quad (16)$$

associated with the continuity equation (10) providing \dot{u} through Eq. (8). We see that, due to Eqs. (13) and (14),

$$\sum_{i=\alpha, \beta, \gamma} \dot{\phi}_i = 0 \quad (17)$$

is locally satisfied at any time in accordance with the constraint in Eq. (4).

On the one hand, for each driving force in Eq. (15), we have a coupling to the conjugate flux $\dot{\phi}_i$ via the phase field dependent timescale $\tau = \tau(\vec{\phi})$, and a cross coupling to the diffusion flux \mathbf{J} via the phase field dependent inverse velocity scale $M = M(\vec{\phi})$. The structure of the cross-coupling term, and especially the reason for introducing the gradient of the phase field, is described in detail in Refs. [15, 16]. On the other hand, for the diffusion driving force, we have a coupling to the conjugate diffusion flux \mathbf{J} via the phase field dependent diffusion coefficient $D = D(\vec{\phi})$, and to the three fluxes $\dot{\phi}_i$ via three cross-coupling terms obeying Onsager symmetry, i.e., parametrized by the same coefficient as in the second term on the right-hand side of Eq. (15). Let us note that when one omits the cross-coupling term in Eq. (15) as in Ref. [11], the model corresponds to the PF model with the so-called anti-trapping current. This model is suited to a one-sided situation for eutectic growth, that does not require Onsager symmetry to be obeyed, as will be seen later. The Onsager relations given above may be represented using a 4×4 (symmetric) matrix, whose determinant should be positive for a positive energy dissipation in the simulated system. Let us note that, while we have defined some phase field dependence of τ, M , and D , we do not assume any for W , that is strictly a constant, yielding isotropic interface energies.

An explicit form of the evolution equations provided by Eqs. (15) and (16) can be obtained from a matrix inversion,

$$\begin{bmatrix} \dot{\phi}_\alpha \\ \dot{\phi}_\beta \\ \dot{\phi}_\gamma \end{bmatrix} = \begin{bmatrix} P_{\alpha\alpha} & P_{\alpha\beta} & P_{\alpha\gamma} \\ P_{\beta\alpha} & P_{\beta\beta} & P_{\beta\gamma} \\ P_{\gamma\alpha} & P_{\gamma\beta} & P_{\gamma\gamma} \end{bmatrix}^{-1} \begin{bmatrix} Q_\alpha \\ Q_\beta \\ Q_\gamma \end{bmatrix}, \quad (18)$$

where, for $i \neq j$,

$$P_{ii} = \tau - D[MW \nabla \phi_i |_{\sum \phi_n=1}]^2, \quad (19)$$

$$P_{ij} = -DM^2 W^2 \nabla \phi_i |_{\sum \phi_n=1} \cdot \nabla \phi_j |_{\sum \phi_n=1}, \quad (20)$$

$$Q_i = -\frac{\delta F}{\delta \phi_i} \Big|_{\sum \phi_n=1} + DMW \nabla \phi_i |_{\sum \phi_n=1} \cdot \nabla u, \quad (21)$$

with

$$\begin{aligned} & -\frac{\delta F}{\delta \phi_i} \Big|_{\sum \phi_n=1} \\ &= HW^2 \nabla^2 \phi_i - \frac{2H}{3} [2\phi_i(1-\phi_i)(1-2\phi_i) \\ & \quad - \phi_j(1-\phi_j)(1-2\phi_j) - \phi_k(1-\phi_k)(1-2\phi_k)] \\ & \quad + \sum_{j=\alpha,\beta,\gamma} (uA_j - B_j) \left[\frac{\partial g_j}{\partial \phi_i}(\vec{\phi}) - \frac{1}{3} \frac{\partial g_j}{\partial \phi_j}(\vec{\phi}) \right] \end{aligned} \quad (22)$$

and

$$\frac{\partial g_i}{\partial \phi_i} = \frac{15\phi_i}{4} [(3\phi_i + 2)(1-\phi_i)^2 + (3\phi_i - 2)(\phi_j - \phi_k)^2], \quad (23)$$

$$\frac{\partial g_i}{\partial \phi_j} = -\frac{\partial g_i}{\partial \phi_k} = \frac{15}{2} \phi_i^2 (1-\phi_i)(\phi_k - \phi_j), \quad (24)$$

for a permutation (i, j, k) of (α, β, γ) .

For the chemical potential, we have

$$\begin{aligned} \dot{u} = \nabla \cdot \left\{ D \left[\nabla u + \sum_{i=\alpha,\beta,\gamma} MW \dot{\phi}_i \nabla \phi_i |_{\sum \phi_n=1} \right] \right\} \\ - \sum_{i=\alpha,\beta,\gamma} \left[A_i(T) \sum_{j=\alpha,\beta,\gamma} \dot{\phi}_j \frac{\partial g_i}{\partial \phi_j}(\vec{\phi}) \right]. \end{aligned} \quad (25)$$

Again, if one sets $M = 0$, the evolution equations presented in Ref. [11] are recovered.

At equilibrium between two phases, for example, between phase i and phase j , the one-dimensional (x is the spatial variable) phase field profile reads

$$\phi_i^{\text{eq}}(x) = 1 - \phi_j^{\text{eq}}(x) = \phi_{\text{eq}}(x) = \frac{1}{2} \left[1 - \tanh \left(\frac{x}{\sqrt{2}W} \right) \right], \quad (26)$$

with $\phi_i^{\text{eq}}(x \rightarrow -\infty) = 1$ and $\phi_i^{\text{eq}}(x \rightarrow \infty) = 0$. The constant chemical potential equals

$$u_{ij}^{\text{eq}} = \frac{B_j - B_i}{A_j - A_i}, \quad (27)$$

and the concentration profile reads

$$c_{ij}^{\text{eq}}(x) = \frac{c_{ij}^0 + c_{ji}^0}{2} + \frac{c_{ij}^0 - c_{ji}^0}{2} \{ 2p[\phi_i^{\text{eq}}(x)] - 1 \}, \quad (28)$$

where c_{ij}^0 (c_{ji}^0) is the concentration in phase i (phase j) when in equilibrium with phase j (phase i).

It is important to generically map (not only for equilibrium) our three-phase field model to the problem of a two-phase system for which a single phase field ϕ is used. The fact that

the variations of two phase fields are involved for a binary interface in our three-phase model brings additional contributions. In particular, the free energy of an interface between phase i and phase j reads now

$$\sigma_{ij} = 2\omega WH, \quad (29)$$

with the factor 2 coming from the fact that two phase fields are exhibiting hyperbolic tangent variations, and with the usual integral $\omega = W \int_{-\infty}^{\infty} [\partial_x \phi_i^{\text{eq}}(x)]^2 dx = \sqrt{2}/6$. We note here that in our fully symmetric model all interface energies are isotropic and equal, i.e., $\sigma_{ij} = \sigma_{jk} = \sigma_{ik}$. As for the classical eutectic growth, our results are expected to be qualitatively unchanged when, while remaining atomically rough, the interfaces present an anisotropic free energy. They are even expected to be quantitatively unchanged in the limit of small anisotropy. Concerning the dynamics, the three-phase field model for a two-phase system reduces to Onsager relations given by

$$-\frac{\delta F}{\delta \phi} = 2\tau \dot{\phi} + (2MW \nabla \phi) \cdot \mathbf{J}, \quad (30)$$

$$-\nabla \frac{\delta F}{\delta c} = (2MW \nabla \phi) \dot{\phi} + \frac{\mathbf{J}}{D}. \quad (31)$$

These are, up to the factors 2 arising from the double contributions of the phase fields, the same Onsager relations presented in Ref. [15] where the kinetic cross coupling parametrized by M was introduced.

Before presenting the thin-interface results that link the parameters of the PF model with sharp interface conditions at the interfaces, let us define the dissipation function. It corresponds to the positive form built out of the products of the driving forces and their respective conjugate flux:

$$\begin{aligned} \dot{S} &= \int_V dV \left(- \sum_{i=\alpha,\beta,\gamma} \frac{\delta F}{\delta \phi_i} \Big|_{\sum \phi_n=1} \dot{\phi}_i - \nabla \frac{\delta F}{\delta c} \cdot \mathbf{J} \right) \\ &= \int_V dV \left\{ \tau \sum_{i=\alpha,\beta,\gamma} (\dot{\phi}_i)^2 \right. \\ & \quad \left. + 2MW \left(\sum_{i=\alpha,\beta,\gamma} \dot{\phi}_i \nabla \phi_i |_{\sum \phi_n=1} \right) \cdot \mathbf{J} + \frac{\mathbf{J}^2}{D} \right\}. \end{aligned} \quad (32)$$

For a binary interface, for example, j/k for which $\phi_i = 0$, $\phi_j = \phi$, $\phi_k = 1 - \phi$, the dissipation reads

$$\dot{S}_{j/k} = \int_V dV \left\{ 2\tau (\dot{\phi})^2 + 4MW \dot{\phi} \nabla \phi \cdot \mathbf{J} + \frac{\mathbf{J}^2}{D} \right\}, \quad (33)$$

and we recover the dissipation function for a PF model with a single phase field ϕ , i.e., $\dot{S} = \int_V dV [(-\delta F/\delta \phi) \dot{\phi} + (-\nabla \delta F/\delta c) \cdot \mathbf{J}]$, with Onsager relations given by Eqs. (30) and (31). The condition of positiveness of the dissipation $\dot{S}_{j/k}$ then reads $2\tau/D - 4M^2 W^2 \phi_{\text{eq}}^2 > 0$.

C. Link with the free-boundary description: Thin-interface limit

In this section, we present the relation between the parameters that enter the PF model and the parameters that enter the sharp interface boundary conditions. This is called the

thin-interface limit of the PF model and allows us to set the PF parameters such that, even with a varying interface width W , the desired boundary conditions are achieved in the equivalent sharp interface model. In particular, at low enough interface velocities, equilibrium boundary conditions may be assumed. We restrict ourselves to the binary interfaces, whereas an analysis of the triple junction is beyond the scope of the paper.

The conservation of atoms A and B at a moving interface between phase i and j implies the relation

$$D_i \nabla c|_i \cdot \mathbf{n} + V c_{ij}^0 = D_j \nabla c|_j \cdot \mathbf{n} + V c_{ji}^0 = J_B. \quad (34)$$

V and J_B are the total normal flux of all atoms through the interface (i.e., the normal velocity) and the normal flux of atoms B through the interface, respectively. If J_A is the normal flux of atoms A, then $V = J_A + J_B$ (we neglect any volume density differences between the phases). The concentration gradient $\nabla c|_i$ ($\nabla c|_j$) is evaluated at the interface on the side of phase i (phase j) and \mathbf{n} is the local unit vector normal to the interface V and J_B are then the scalar products of the actual fluxes and \mathbf{n} . D_i (D_j) is the bulk diffusion coefficient in phase i (phase j). Here, we have assumed weak out-of-equilibrium conditions such that the concentration in phase i (phase j) that enters the mass conservation equations is the equilibrium concentration c_{ij}^0 (c_{ji}^0).

Together with mass conservation, kinetic boundary conditions are defined. They relate linearly the jumps $\delta\Omega$ and δu across the interface of the grand potential and the chemical potential (rigorously the diffusion potential), respectively, to the two fluxes V and J_B . These boundary conditions involve the bulk free energies $f_i(c)$ and $f_j(c)$ of the two phases and especially their second derivatives at i/j equilibrium [which is equal to 1 for the parabolic free energies in Eq. (6)]. They prescribe the interface concentrations c_{ij} and c_{ji} when the sharp interface problem is solved, according to $\delta\Omega = f_j''(c_{ji}^0)c_{ji}^0(c_{ji} - c_{ji}^0) - f_i''(c_{ij}^0)c_{ij}^0(c_{ij} - c_{ij}^0)$ and $\delta u = f_i''(c_{ij}^0)(c_{ij} - c_{ij}^0) - f_j''(c_{ji}^0)(c_{ji} - c_{ji}^0)$. Consequently, the kinetic boundary conditions are written as

$$\delta\Omega = \bar{A}V + \bar{B}J_B + d_0\kappa, \quad (35)$$

$$\delta u = \bar{B}V + \bar{C}J_B, \quad (36)$$

where \bar{A} , \bar{B} , \bar{C} are the components of the 2×2 Onsager matrix of kinetic coefficients, d_0 is the capillary length (as mentioned in Sec. II A, the relation between the capillary length and the interface width in the present PF model is given by $d_0/W = 2\omega H/X$), and κ the curvature of the interface. In the following we present the strategy to achieve equilibrium boundary conditions, i.e., $\delta\Omega = 0$ and $\delta u = 0$, even when V and J_B do not vanish. In this case one recovers the Gibbs-Thomson relation,

$$c_{ij} - c_{ij}^0 = (c_{ji} - c_{ji}^0)f_j''/f_i'' = -\tilde{d}\kappa, \quad (37)$$

where

$$\tilde{d} = \frac{d_0}{(c_{ij}^0 - c_{ji}^0)f_i''}. \quad (38)$$

The equilibrium concentrations c_{ij}^0 and c_{ji}^0 are temperature dependent through A_i and B_i .

In Ref. [17], the general expressions for the kinetic coefficients \bar{A} , \bar{B} , and \bar{C} in terms of the PF model equilibrium properties were derived. For our equilibrium i/j interface centered at $x = 0$, we have $\phi_i(x) = \phi_{\text{eq}}(x)$ given by Eq. (26), $\phi_j(x) = 1 - \phi_{\text{eq}}(x)$, and $\phi_k(x) = 0$. Furthermore, we have $c(x) = c_{\text{eq}}(x) = (c_{ij}^0 + c_{ji}^0)/2 + \{(c_{ij}^0 - c_{ji}^0)/2\}\{2p[\phi_{\text{eq}}(x)] - 1\}$ given by Eq. (28). Here, we note that, since $p(\phi) = \phi^3(10 - 15\phi + 6\phi^2)$, $2p - 1$ is an odd function of x . Taking into account the double contribution of the phase fields at binary interfaces, the kinetic coefficients read

$$\begin{aligned} \bar{A} &= 2 \int_{-\infty}^{\infty} \tau [\phi'_{\text{eq}}(x)]^2 dx - 4 \int_{-\infty}^{\infty} \{MW[\phi'_{\text{eq}}(x)]^2 c_{\text{eq}}(x)\} dx \\ &+ \int_{-\infty}^{\infty} \left\{ \frac{c_{\text{eq}}^2(x)}{D} - \frac{(c_{ij}^0)^2}{2D_i} - \frac{(c_{ji}^0)^2}{2D_j} \right\} dx, \end{aligned} \quad (39)$$

$$\begin{aligned} \bar{B} &= 2 \int_{-\infty}^{\infty} \{MW[\phi'_{\text{eq}}(x)]^2\} dx \\ &- \int_{-\infty}^{\infty} \left\{ \frac{c_{\text{eq}}(x)}{D} - \frac{c_{ij}^0}{2D_i} - \frac{c_{ji}^0}{2D_j} \right\} dx, \end{aligned} \quad (40)$$

$$\bar{C} = \int_{-\infty}^{\infty} \left\{ \frac{1}{D} - \frac{1}{2D_i} - \frac{1}{2D_j} \right\} dx. \quad (41)$$

We recall at this point that in these expressions $\tau = \tau(\vec{\phi})$, $M = M(\vec{\phi})$, and $D = D(\vec{\phi})$, which we have not specified yet.

For a two-phase PF model with a single phase field ϕ , it was shown that constant τ and M are sufficient to achieve the desired boundary conditions, both for a one-sided [17] and a two-sided model [16]. Here, for the three-phase model, the necessity for the constraint in Eq. (4) to be fulfilled imposes that $\tau(\vec{\phi})$ and $M(\vec{\phi})$, as single quantities, contain enough information for the properties of the three kinds of interfaces to be ascribed independently. We have chosen the following forms with six parameters:

$$\tau(\vec{\phi}) = \tau_{\alpha\beta}(1 + \phi_\alpha\phi_\beta) + \tau_{\beta\gamma}(1 + \phi_\beta\phi_\gamma) + \tau_{\gamma\alpha}(1 + \phi_\gamma\phi_\alpha), \quad (42)$$

$$M(\vec{\phi}) = M_{\alpha\beta}\phi_\alpha\phi_\beta + M_{\beta\gamma}\phi_\beta\phi_\gamma + M_{\gamma\alpha}\phi_\gamma\phi_\alpha. \quad (43)$$

The diffusion coefficient $D(\vec{\phi})$ should be able to reproduce the three different bulk diffusion coefficients but also to allow for a tuning of the effective surface diffusion coefficient that arises due to the finiteness of the interface width W [18]. As shown in Ref. [16], the phase field dependent diffusion coefficient appears as a harmonic mean in order for \bar{C} to vanish. Here, we define

$$\frac{1}{D(\vec{\phi})} = \frac{1}{3} \sum_{i=\alpha,\beta,\gamma} \left\{ \frac{1}{D_i} + h_i(\vec{\phi}) \left(\frac{1}{D_i} - \frac{1}{2D_j} - \frac{1}{2D_k} \right) \right\}, \quad (44)$$

where

$$h_i(\vec{\phi}) = (2\phi_i - 1)(1 + 4a_{ij}\phi_i\phi_j + 4a_{ik}\phi_i\phi_k), \quad (45)$$

for a permutation (i, j, k) of (α, β, γ) .

We have here three additional parameters a_{ij} . We will see in the following how the assumptions of equilibrium boundary

conditions and vanishing surface diffusion allow us to determine the nine parameters τ_{ij} , M_{ij} , a_{ij} .

For a binary i/j interface, $D_{i/j}(\phi) = D(\phi_i = \phi, \phi_j = 1 - \phi, \phi_k = 0)$ is such that

$$\frac{1}{D_{i/j}(\phi)} = \frac{1}{2D_i} + \frac{1}{2D_j} + h_{i/j}(\phi) \left(\frac{1}{2D_i} - \frac{1}{2D_j} \right), \quad (46)$$

where

$$h_{i/j}(\phi) = (2\phi - 1)[1 + 4a_{ij}\phi(1 - \phi)]. \quad (47)$$

This is precisely the phase field dependent diffusion coefficient that was used in the two-phase model presented in Ref. [18]. Let us however note that in Ref. [18] ϕ varies from -1 to 1 , while here it is in the range $0-1$. The factor 4 in $h_{i/j}(\phi)$ then allows a_{ij} to be identified with a in Ref. [18].

Returning to our calculation of the kinetic coefficients given in Eqs. (39)–(41), we find for the i/j interface

$$\begin{aligned} \bar{A} = 2 \frac{\omega(\tau_{\alpha\beta} + \tau_{\beta\gamma} + \tau_{\gamma\alpha}) + \chi\tau_{ij}}{W} \\ - \frac{\zeta(c_{ij}^0 - c_{ji}^0)^2}{4} \left(\frac{W}{2D_i} + \frac{W}{2D_j} \right), \end{aligned} \quad (48)$$

$$\bar{B} = 2\chi M_{ij} - \frac{\varrho_{ij}(c_{ji}^0 - c_{ij}^0)}{2} \left(\frac{W}{2D_i} - \frac{W}{2D_j} \right), \quad (49)$$

$$\bar{C} = 0, \quad (50)$$

where

$$\chi = W \int_{-\infty}^{\infty} \phi_{\text{eq}} [1 - \phi_{\text{eq}}] [\phi'_{\text{eq}}]^2 dx \approx 0.04714, \quad (51)$$

$$\zeta = \frac{1}{W} \int_{-\infty}^{\infty} (1 - \{2p[\phi_{\text{eq}}] - 1\}^2) dx \approx 1.40748, \quad (52)$$

$$\varrho_{ij} = \frac{1}{W} \int_{-\infty}^{\infty} \{1 - [2p(\phi_{\text{eq}}) - 1]h_{i/j}(\phi_{\text{eq}})\} dx. \quad (53)$$

As mentioned above, \bar{C} vanishes, and this is due to the oddness of $h_{i/j}(\phi_{\text{eq}})$, i.e., the oddness of $2\phi_{\text{eq}} - 1$. In order to achieve equilibrium boundary conditions at the i/j interface, i.e., having $\delta\Omega = 0$ and $\delta u = 0$ in Eqs. (35) and (36), we need also $\bar{A} = 0$ and $\bar{B} = 0$. Moreover, we want to achieve equilibrium conditions also at the j/k and the k/i interfaces. The condition $\bar{A} = 0$ at each interface yields three equations for the three parameters $\tau_{\alpha\beta}$, $\tau_{\beta\gamma}$, $\tau_{\gamma\alpha}$,

$$\begin{aligned} \chi\tau_{ij} + \omega(\tau_{\alpha\gamma} + \tau_{\alpha\beta} + \tau_{\beta\gamma}) \\ = \frac{\zeta(c_{ij}^0 - c_{ji}^0)^2}{8} \left(\frac{W^2}{2D_i} + \frac{W^2}{2D_j} \right) = A_{ij}, \end{aligned} \quad (54)$$

where i, j, k are pairwise different, and the solution for τ_{ij} reads

$$\tau_{ij} = \frac{1}{\chi} \left[A_{ij} - \frac{\omega}{3\omega + \chi} (A_{\alpha\gamma} + A_{\alpha\beta} + A_{\beta\gamma}) \right]. \quad (55)$$

On the other hand, $\bar{B} = 0$ at the three interfaces yields three more equations,

$$M_{ij} = \frac{\varrho_{ij}(c_{ji}^0 - c_{ij}^0)}{4\chi} \left(\frac{W}{2D_i} - \frac{W}{2D_j} \right). \quad (56)$$

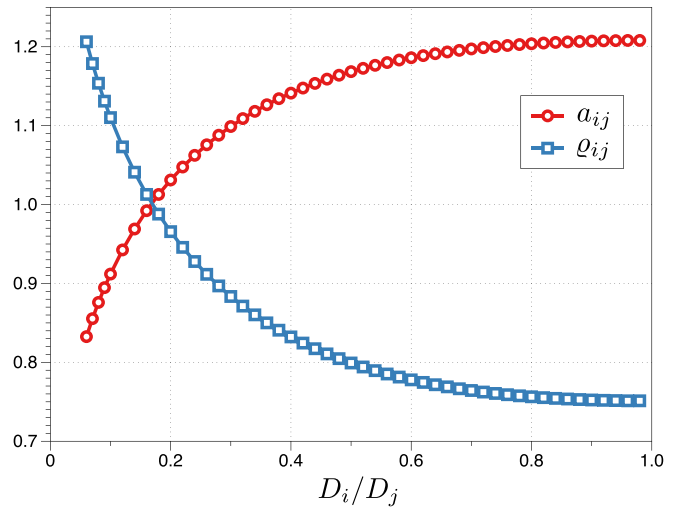


FIG. 1. Selected parameter a_{ij} in the range $0.06 < D_i/D_j < 1$ to eliminate the surface diffusion and corresponding value of ϱ_{ij} .

We note here that no cross coupling is necessary, i.e., $M_{ij} = 0$, when $D_i = D_j$. In the general case, M_{ij} does not vanish and depends on ϱ_{ij} , that remains to be determined. This is achieved by the assumption of a vanishing surface diffusion coefficient, through the determination of a_{ij} . This corresponds to the condition

$$\int_{-\infty}^{\infty} dx \left(D_{i/j}(\phi_{\text{eq}}) - \frac{D_i}{2} - \frac{D_j}{2} \right) = 0. \quad (57)$$

This gives three additional equations in order to be able to fully determine the nine aforementioned parameters. The coefficient a_{ij} that satisfies Eq. (57) is a function of the ratio D_i/D_j , and it has the property $a_{ij}(D_i/D_j) = a_{ij}(D_j/D_i)$ [14]. Hence, we have also $\varrho_{ij}(D_i/D_j) = \varrho_{ij}(D_j/D_i)$. In Fig. 1, we present the values of a_{ij} and ϱ_{ij} as a function of $D_i/D_j > 0.06$.

Let us give a brief comment before presenting the one-sided model. We have seen that the condition of positiveness of the dissipation corresponds to the inequality $2\tau/D - 4M^2W^2\phi_{\text{eq}}^2 > 0$, and thus the magnitude of M may not be too large. When considering equilibrium boundary conditions, this inequality sets an upper bound for the contrast D_i/D_j beyond which M is too large. According to our definition of $\tau(\vec{\phi})$, τ_{ij} is a function of all three diffusion coefficients [see Eq. (55)] and the maximum contrast D_i/D_j depends on the other contrasts D_i/D_k and D_j/D_k . In this respect, more suitable definitions of $\tau(\vec{\phi})$ may be used. In Fig. 1, $D_i/D_j = 0.06$ corresponds roughly to the maximum contrast that is used in the simulations in the following section, i.e., $D_j/D_i = 15$.

One-sided model. In this paper, we present simulations for a negligible diffusion coefficient in the growing phases α and β ($D_\alpha, D_\beta \ll D_\gamma$). In the PF model, we then use

$$\tau_{\alpha\beta} = 0, \quad (58)$$

$$M_{\alpha\beta} = 0, \quad (59)$$

$$D(\vec{\phi}) = D_{1s}(\vec{\phi}) = D_\gamma(1 - \phi_\alpha - \phi_\beta). \quad (60)$$

In the mass conservation equation (34) for an interface between the mother phase γ and one of the growing phases j ($j = \alpha, \beta$), the diffusion flux in the growing phase vanishes, yielding

$$Vc_{j\gamma}^0 = J_B. \quad (61)$$

The kinetic boundary conditions (35) and (36) become

$$\delta\Omega = (\bar{A} + c_{j\gamma}^0\bar{B})V + d_0\kappa, \quad (62)$$

$$\delta u = (\bar{B} + c_{j\gamma}^0\bar{C})V. \quad (63)$$

The two fluxes V and J_B are no longer linearly independent, and Onsager symmetry becomes irrelevant since, for example, two driving forces are expressed in terms of a single flux. As mentioned earlier, this allows us to use the PF model with the so-called antitrapping current.

In view of Eqs. (62) and (63), the assumption of equilibrium boundary conditions thus demands $\bar{A} + c_{j\gamma}^0\bar{B} = 0$ and $\bar{B} + c_{j\gamma}^0\bar{C} = 0$. According to Eqs. (39)–(41), we have

$$\bar{A} + c_{j\gamma}^0\bar{B} = 2\frac{(\omega + \chi)\tau_{j\gamma} + \omega\tau_{k\gamma}}{W} - \frac{(c_{\gamma j}^0 - c_{j\gamma}^0)^2 W \xi}{4D_\gamma}, \quad (64)$$

$$\bar{B} + c_{j\gamma}^0\bar{C} = 2\chi M_{j\gamma} - \frac{(c_{\gamma j}^0 - c_{j\gamma}^0)W\kappa}{2D_\gamma}, \quad (65)$$

where

$$\kappa = \frac{1}{W} \int_{-\infty}^{\infty} \frac{\phi_{\text{eq}} + 1 - 2p[\phi_{\text{eq}}]}{1 - \phi_{\text{eq}}} dx \approx 2.12132, \quad (66)$$

$$\xi = \frac{1}{W} \int_{-\infty}^{\infty} \frac{1 - (2p[\phi_{\text{eq}}] - 1)^2}{1 - \phi_{\text{eq}}} dx \approx 3.42778. \quad (67)$$

The assumption of equilibrium boundary conditions at interfaces α/γ and β/γ provides four equations for $\tau_{\alpha\gamma}$, $\tau_{\beta\gamma}$, $M_{\alpha\gamma}$, $M_{\beta\gamma}$ ($j = \alpha, \beta, k \neq j$),

$$M_{j\gamma} = \frac{(c_{\gamma j}^0 - c_{j\gamma}^0)W\kappa}{4\chi D_\gamma}, \quad (68)$$

and

$$(\omega + \chi)\tau_{j\gamma} + \omega\tau_{k\gamma} = \frac{(c_{\gamma j}^0 - c_{j\gamma}^0)^2 W^2 \xi}{8D_\gamma} = A_j^{1s}, \quad (69)$$

yielding

$$\tau_{j\gamma} = \frac{1}{\chi} \left[A_j^{1s} - \frac{\omega}{2\omega + \chi} (A_\alpha^{1s} + A_\beta^{1s}) \right]. \quad (70)$$

Here, for an interface j/γ for which $\phi_j(x) = \phi_{\text{eq}}(x)$, we have $D = 1 - \phi_{\text{eq}}$ and surface diffusion is automatically eliminated, i.e., $\int_{-\infty}^{\infty} (D - D_\gamma/2) dx = (D_\gamma/2) \int_{-\infty}^{\infty} (1 - 2\phi_{\text{eq}}) dx = 0$.

III. SIMULATION DETAILS

To investigate the capabilities of the nondiagonal three-PF model during eutectic and eutectoid transformations, we perform two-dimensional simulations of lamellar steady-state growth with different diffusivities in the growing phases, and different global compositions C_∞ , i.e., different compositions in the mother phase far ahead of the growth front. In dimensionless units we thus define $c_\infty = (C_\infty - C_E)/(C_\beta -$

$C_\alpha)$. In a first step we perform simulations corresponding to eutectic directional solidification (with one-sided diffusion). The scaled undercooling at the steady-state growth front is extracted from simulations and benchmarked against the boundary integral calculations reported in Ref. [11]. In a second step we perform simulations of isothermal transformations in the two-sided case. The nondiagonal PF simulation results are analyzed in the frame of the extended Jackson-Hunt theory by Ankit *et al.* [6] for various lamellar spacings λ at the eutectoid and one off-eutectoid compositions.

The simulation boxes of total size $n_x \times n_y$ with the grid spacing $\Delta x = \Delta y = 0.4W$ are illustrated in Figs. 2(a) and 2(b), where n_x and n_y are the length of simulation boxes in the direction parallel and perpendicular to the solidification front. We require $\lambda \leq 0.1n_y$ to ensure that the simulation domain is large enough in order to describe the diffusion field in the parent phase. For the purpose of obtaining steady-state periodic lamellar arrays, periodic boundary conditions are prescribed at the boundaries parallel to the growth direction, while no-flux boundary conditions are used at the boundaries perpendicular to the growth direction (see Fig. 2). Also, a moving-frame method and GPU acceleration are applied in the simulations to reduce the computational effort.

Following Ref. [11], we assume for the symmetric phase diagram that $A_\gamma = B_\gamma = 0$, that the A_i 's are independent of the temperature T , i.e.,

$$A_\alpha = -A_\beta = -0.5, \quad (71)$$

and that

$$B_\alpha = A_\alpha \Delta = B_\beta = -A_\beta \Delta. \quad (72)$$

In this way, the concentration of phase i in equilibrium with phase j reads $c_{ij}^0 = A_i + (B_j - B_i)/(A_j - A_i)$. Explicitly, this gives

$$c_{\alpha\beta}^0 = -c_{\beta\alpha}^0 = A_\alpha, \quad (73)$$

$$c_{\gamma\alpha}^0(T) = c_{\alpha\gamma}^0(T) - A_\alpha = -c_{\gamma\beta}^0(T) = A_\beta - c_{\beta\gamma}^0(T) = \Delta, \quad (74)$$

where $\Delta = \frac{T_E - T}{m(C_\beta - C_\alpha)}$ with $m > 0$ the liquidus slope. Thus Δ is the dimensionless undercooling. The corresponding phase diagram is schematically presented in Fig. 2(c). In a positive thermal gradient in the z direction, we have $\Delta = (z_E - z)/l_T$, where z_E is the position of the eutectic and eutectoid temperature and $l_T > 0$ denotes the corresponding thermal length.

In the first step corresponding to eutectic directional solidification, we choose three different values for λ_e/W , i.e., $\lambda_e/W = 64, 96$, and 128 , where λ_e is the Jackson-Hunt spacing (corresponding to the minimum undercooling) given in Eq. (2.17) in Ref. [11] (recall that here $\sin \theta_\alpha = \sin \theta_\beta = 1/2$), i.e., $\lambda_e = \sqrt{l_D \bar{d}/P(\eta)}$, where $l_D = D_\gamma/V$ and the polynomial $P(\eta) = \sum_{n=1}^{\infty} \sin^2(\pi \eta n)/(\pi n)^3$ depends on the phase fraction $\eta = (c_{\beta\alpha}^0 - c_\infty)/(c_{\beta\alpha}^0 - c_{\alpha\beta}^0)$ of phase α (which is $1/2$ at eutectic composition). For each of these values, we then choose \bar{d} and l_D such that $l_D/\bar{d} = 51200$. The thermal gradient is chosen such that $l_T/l_D = 4$.

In the second step corresponding to isothermal eutectoid transformations, we prescribe $\bar{d}/W = 0.5$ and an undercooling $\Delta = 0.03125$ [see Eq. (74)]. This gives λ_e such that,

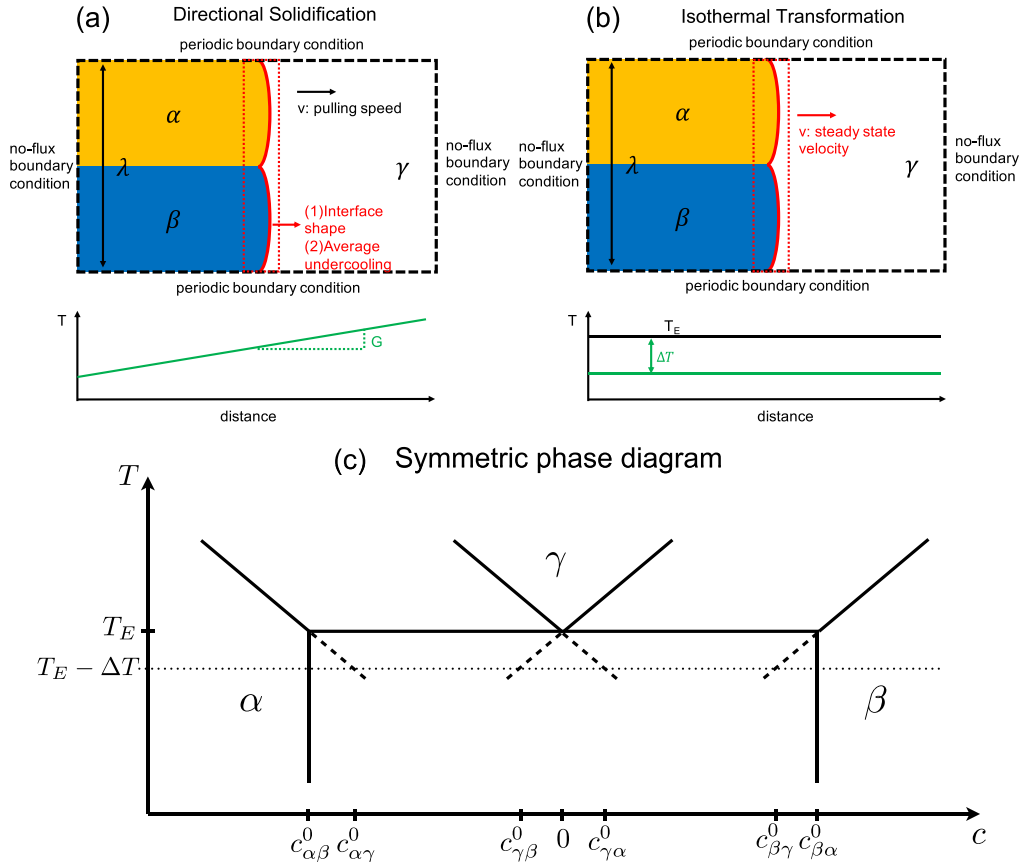


FIG. 2. (a) and (b) show the schematic step of the simulations during directional solidification and during isothermal transformations, respectively. (c) Symmetric phase diagram for eutectic and eutectoid transformations.

according to $\lambda_e = \tilde{d}/[\eta(1-\eta)\Delta]$, $\lambda_e/W = 64$ for $c_\infty = 0$ (i.e., $\eta = 0.5$), and $\lambda_e = 66.6667$ for $c_\infty = 0.1$ (i.e., $\eta = 0.4$).

IV. RESULTS AND DISCUSSIONS

A. Verification of the nondiagonal PF model in the one-sided case

In the present section, we perform nondiagonal PF [NPF, i.e., with the cross-coupling term $M(\vec{\phi})$] and classical PF [CPF, $M(\vec{\phi}) = 0$] simulations in the one-sided case for different lamellar spacings, $\lambda = \lambda_e = 64W$, $96W$, and $128W$, during directional solidification. λ_e is related to the spacing with the minimum interface undercooling for directional solidification and to the maximum growth velocity for isothermal solidification. We extract the scaled interface shapes in a steady state from the PF simulations and benchmark them with boundary integral (BI) calculations, as presented in Fig. 3(a). The position z is the distance to the eutectic temperature, that lies ahead at a higher temperature, and is normalized by the thermal length l_T . As can be seen, when the abnormal interface effects are eliminated in the NPF simulations, the quantitative agreement with the BI calculation is significantly improved compared to the CPF simulations. We quantify this improvement in Fig. 3(b) where we give the deviation of the lamella's tip position in the PF simulations from the one obtained in the BI calculation. Let us note also that, as the

inset in Fig. 3(a) and the dependence on W/λ_e in Fig. 3(b) show, we obtain a better agreement with the BI method when a better separation of the length scale is achieved, i.e., when λ_e/W increases.

Next, using the parameters as aforementioned, a series of NPF simulations is performed at $\lambda = \lambda_e$ for various λ_e during directional solidification. The dependence on the lamellar spacing of the extracted average interface undercooling in the steady-state regime can then be compared with the Jackson-Hunt theory and is exhibited in Fig. 4. As can be seen from the comparison, there exists a 5%–7% discrepancy with the JH theory, due to the assumption of a flat solidification front in the latter theory. In addition, we also show the results from Ref. [11] in Fig. 4. We see a slight discrepancy with our NPF results, certainly due to the fact that we use a symmetric matrix in the force-flux Onsager relations, while only the antitrapping current is present in the model used in Ref. [11] [see the brief discussion immediately after Eq. (63)]. Overall, the capabilities of the NPF model for eutectics, i.e., when diffusion in the growing phases is inhibited, are demonstrated.

B. Comparison of the nondiagonal PF model with the extended JH theory in the two-sided case

In this section, we investigate the case where diffusion is also present in the growing phases, i.e., where $\mu_\alpha = D_\alpha/D_\gamma$ and $\mu_\beta = D_\beta/D_\gamma$ are finite. As mentioned in the Introduction,

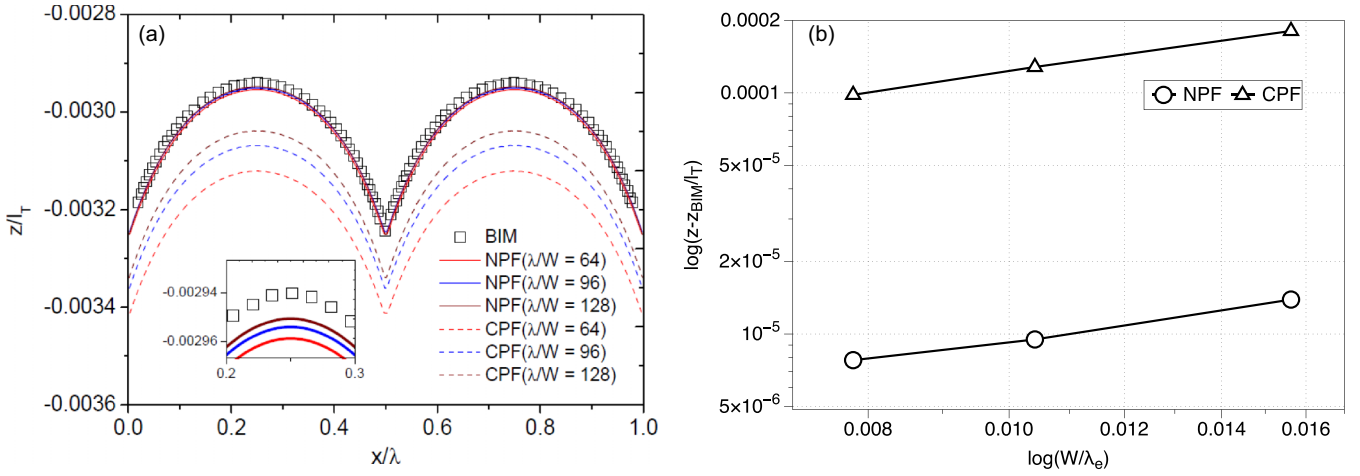


FIG. 3. (a) Comparison between NPF (solid lines) and CPF (dashed lines) simulation results with the boundary integral method (BIM, squares) taken from Ref. [11] for $\lambda_e/W = 64, 96$, and 128 . Inset: Enlargement of the dashed rectangle. (b) Deviation of the lamella's tip position ($x/\lambda = 0.25$) between NPF and CPF simulation results and BI calculations.

an extension of the JH theory was developed [6] in order to take into account these additional ingredients in the dynamics of the system. Within this theory, diffusion fluxes in the growing phases are simply added to the flux in the mother phase, and in isothermal conditions, the velocity

$$V = V_{\text{JH}}\rho \quad (75)$$

is multiplied by the factor ρ given in Eq. (3). For our symmetric phase diagram, we have

$$\rho = 1 + A[\mu_\alpha\eta + \mu_\beta(1 - \eta)], \quad (76)$$

where A is described as a factor related to the difference in solidus and liquidus slopes. First we perform simulations for $\mu_\alpha = \mu_\beta$. The cross-coupling parameter $M_{\alpha\beta}$ thus vanishes and surface diffusion is automatically suppressed at the α/β interface [there is no need to adjust the coefficient $Q_{\alpha\beta}$ —see

the discussion following Eq. (56)]. Moreover, we use $c_\infty = 0$ ($\eta = 0.5$), yielding a fully symmetric pattern. We investigate the dependence of the growth velocity on λ (we recall that $\lambda_e/W = 64$ and $\tilde{d}/W = 0.5$).

Since the extension of the JH theory in Ref. [6] is only approximate, at least because it neglects some curvature effects just as Jackson and Hunt do, we have decided to determine A by choosing the value for which Eq. (75) best fits our simulations results for $\mu_\alpha = \mu_\beta = 1$. We found $A = 0.8924$.

In order to investigate the relevance of the scaling proposed by Eq. (75), we plot in Fig. 5 the rescaled dimensionless velocity

$$\tilde{V} = \frac{V\lambda_e}{D_\gamma} \frac{1}{\rho} \quad (77)$$

as a function of λ for $0 \leq \mu \leq 15$ where $\mu = \mu_\alpha = \mu_\beta$. Here, we thus have $\rho = 1 + 0.8924\mu$. The solid line corresponds to

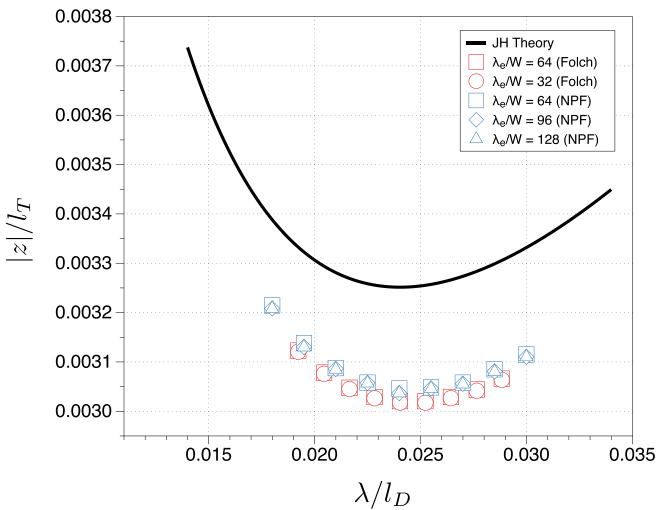


FIG. 4. Comparison between the PF simulation results and Jackson-Hunt theory during directional solidification for different λ_e/W . The solid line is the Jackson-Hunt theory. The blue points present the NPF results. The red points indicate the results taken from Ref. [11].

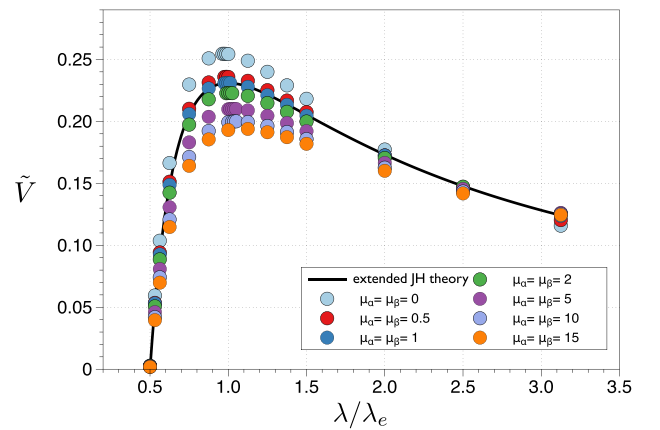


FIG. 5. Rescaled dimensionless growth velocities obtained from NPF simulations for different lamellar spacings with a varying diffusion coefficient being equal in the growing phases, i.e., $0 \leq \mu \leq 15$ ($\mu = \mu_\alpha = \mu_\beta$). The solid lines corresponds to $\mu = 1$ (see text). The relatively small amplitude of the scattering of the results for a given λ validates the relevance of Eq. (75) to predict the velocity as a function of μ .

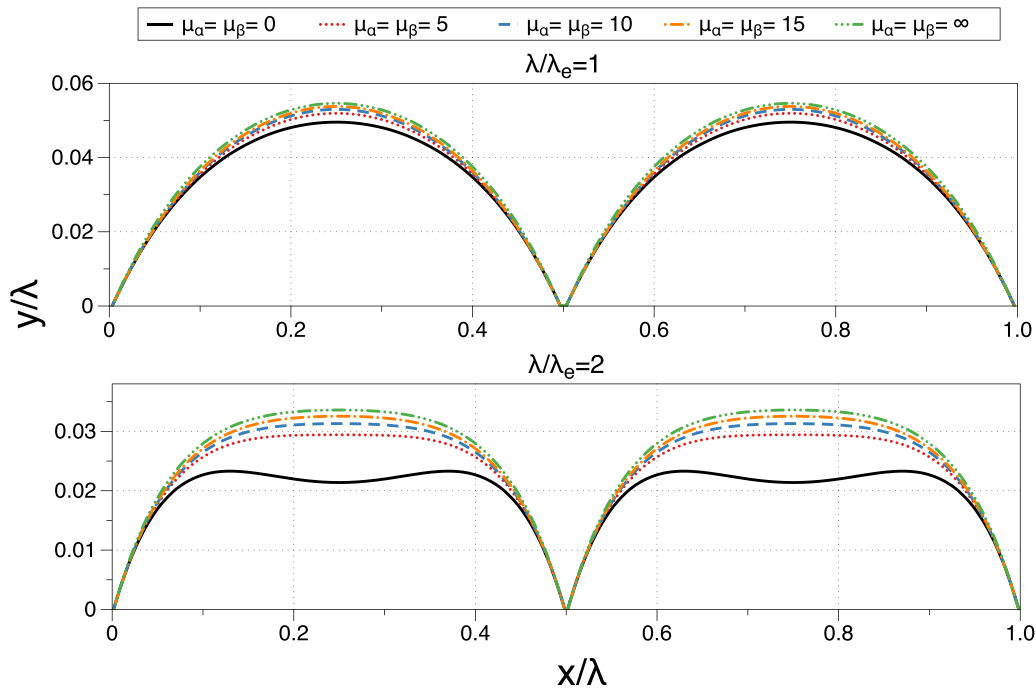


FIG. 6. The scaled shapes of the growth fronts extracted from the NPF simulation results for $\mu_\alpha = \mu_\beta = 0, 5, 10, 15, \infty$ and $\lambda/\lambda_e = 1, 2$.

the reference case, i.e., $\mu = 1$, that provides through the fit the quantity ρ (through A) by which we divide the velocity. We clearly observe a scattering of the simulations results around the solid line, showing that \tilde{V} is not independent of μ . However, the relatively small amplitude of this scattering demonstrates that Eq. (75) provides a very good prediction of the velocity. Indeed, in view of the fact that μ spans a huge range within which the velocity is multiplied by a factor close to 15, a discrepancy of at most 30% for \tilde{V} between the cases $\mu = 0$ and $\mu = 15$ corresponds to a rather convincing data collapse. If the arguments developed in Ref. [6] were inappropriate and, for example, diffusion would not take place in the growing phases even if their diffusion coefficient is large, the velocity would not change much when this diffusion coefficient increases, and \tilde{V} would end up close to 0.01 at $\lambda/\lambda_e = 1$. The situation here is very different.

When we look, for a given λ , at the dependence of \tilde{V} on μ , our simulations suggest that it converges when μ becomes large. When $\mu \gg 1$, i.e., when the diffusion coefficient in the growing phases α and β is much larger than the one in the mother phase γ , the main diffusion path is within the growing phases and the diffusion fluxes in the mother phase become negligible. Then, $\rho \sim \mu$, and the steady-state velocity becomes proportional to $D_\alpha = D_\beta$ according to $V/D_\gamma \sim \rho \sim D_{\alpha(\beta)}/D_\gamma$. Thus, V exhibits a linear variation with μ (i.e., \tilde{V} becomes independent of μ) when $\mu \gg 1$, and the shape of the interfaces becomes self-similar. This is what we see in Fig. 6, where we plot the shape of the α/γ and β/γ interfaces (we recall that due to symmetry the α/β interface is straight behind the triple junction) for $\lambda/\lambda_e = 1$ and $\lambda/\lambda_e = 2$, and for $\mu = 0, 5, 10$, and 15 . We also plot the shape that is obtained for the case where μ is formally infinite, i.e., when D_γ is strictly vanishing (we then use the one-sided model). This situation is at odds with the usual assumption for eutectic growth, and we are not aware of any description of such a

steady state in the literature. Let us note that we have checked that this scenario exists also for off-eutectoid concentrations, showing that the existence of the steady state is not restricted to high-symmetry conditions.

On the other hand, since $\rho = 1 + A\mu$, $V - V_{\text{JH}}$ varies linearly with μ when $\mu \ll 1$. We exhibit these two linear regimes in Fig. 7 where we plot our simulations results (squares)

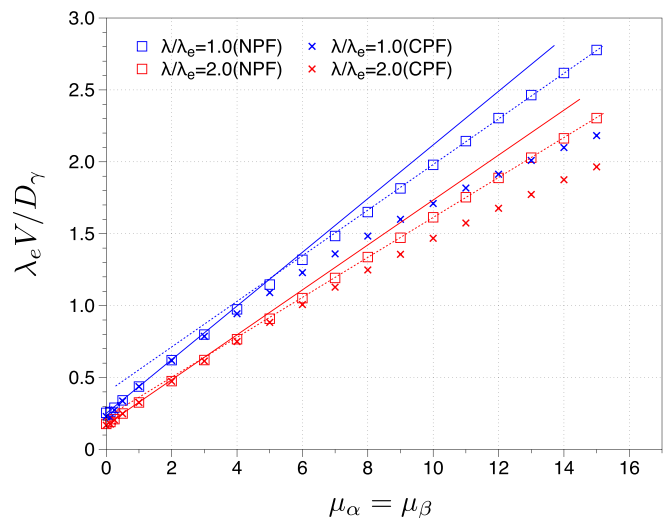


FIG. 7. Dimensionless velocity obtained with the nondiagonal PF model (NPF, squares) and the classical PF model (CPF, crosses) as a function of the diffusion coefficient in the growing phases $\mu_\alpha = \mu_\beta$ for two different lamellar spacings $\lambda/\lambda_e = 1$ and 2 . The solid lines illustrate the small μ linear regime for which the steady-state velocity is proportional to the diffusion coefficient in the mother phase γ and the dashed lines illustrate the large μ linear regime for which the velocity scales as the diffusion coefficient in the growing phases.

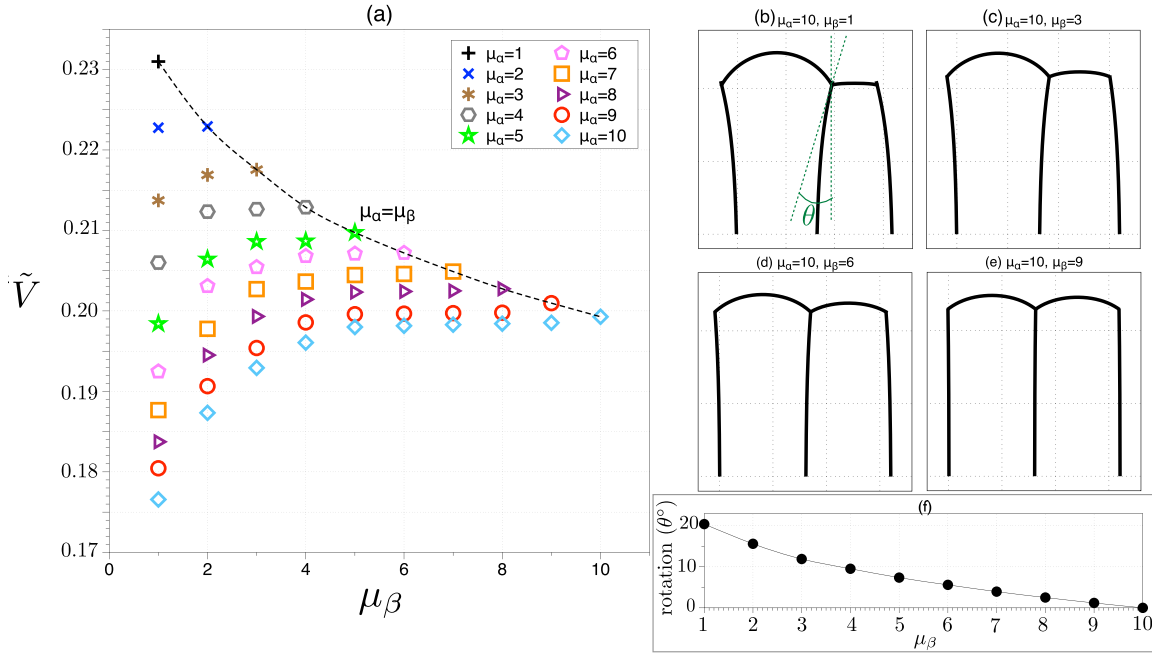


FIG. 8. (a) Rescaled dimensionless growth velocities obtained from NPF simulations during an isothermal transformation at the eutectoid composition and $\lambda = \lambda_e$, with unequal μ_α and μ_β (the dashed line corresponds to $\mu_\alpha = \mu_\beta$). (b)–(j) show the alteration of the lamellar shapes extracted from NPF results for $\mu_\alpha = 10$, $\mu_\beta = 1$ –9, respectively. (k) The rotation angle (θ) of the triple junction in (b)–(j).

for $V\lambda_e/D_\gamma$ as a function of μ for $\lambda/\lambda_e = 1$ and 2. We see that close to the origin we may approximate our results by the straight solid lines, and that this linear regime actually extends to values of μ of order unity. As mentioned before, the diffusivity ratio μ may not be too small due to the stability constraints. Moreover, small μ simulations show minor inaccuracies owing to the sharp variations across the interface of the function that allows for elimination of surface diffusion h_i . Note that a tensorial diffusivity [22] has been proposed as an alternative to h_i in Ref. [23], and according to the authors no constraint on the diffusivity ratio then exists.

Complementary, when μ is large enough, our results are well approximated by the dashed straight lines. In the same plot in Fig. 7, we also display the results (crosses) that one obtains for the classical PF model (CPF). We see that the larger μ , the larger the discrepancy between the NPF and CPF models, indicating the importance of the cross-coupling terms parametrized by $M(\vec{\phi})$.

C. Influence of the different diffusivity ratios of growing phases on the lamellar growth patterns at eutectoid and off-eutectoid composition

Let us now investigate the situation where the three diffusion coefficients are different, i.e., $\mu_\alpha \neq \mu_\beta$ (here, all cross-coupling terms M_{ij} are thus nonvanishing and surface diffusion should be eliminated at each interface, i.e., all values ρ_{ij} should be adjusted).

We first perform simulations at $c_\infty = 0$ and $\lambda/\lambda_e = 1$. In Fig. 8, we present \tilde{V} for $\mu_\beta \leq \mu_\alpha$ (owing to the choice $c_\infty = 0$, the velocity is invariant under an exchange of μ_α and μ_β). The coefficient A in the expression for ρ is the same as in the previous study, i.e., $\rho = 1 + 0.8924(\mu_\alpha + \mu_\beta)/2$. The

dashed line represents the results corresponding to $\mu_\alpha = \mu_\beta$. Again, we observe some scattering of the results showing that \tilde{V} is not strictly independent of ρ . However, the amplitude of this scattering, that reaches at most around 30% for $\mu_\beta = 1$, is still much smaller than the variation of ρ , demonstrating that Eq. (75) is able to predict quite faithfully the steady-state velocity as a function of μ_α and μ_β .

Even though $c_\infty = 0$, the pattern is nonsymmetric owing to $\mu_\alpha \neq \mu_\beta$. In particular, as can be seen in Figs. 8(b)–8(e), where we present the interfaces shapes for different ratios μ_β/μ_α and $\mu_\alpha = 10$, the α/β interface forms a finite angle with the vertical direction, and we denote it as θ at the triple junction. In Fig. 8(f), we plot θ (in degrees) as a function of μ_β ($1 \leq \mu_\beta \leq 10$) for $\mu_\alpha = 10$. It decreases when μ_β increases and vanishes at $\mu_\beta = \mu_\alpha$ as expected for a fully symmetric pattern.

Let us now investigate a case where the composition is off-eutectoid, i.e., $c_\infty = 0.1$. Then $\eta = 0.4$ and $\rho = 1 + A(0.4\mu_\alpha + 0.6\mu_\beta)$. Here, the best fit to our simulation results for $\mu_\alpha = \mu_\beta = 1$ gives $A = 0.8989$. We use this value to calculate the rescaled dimensionless velocity \tilde{V} , and we plot the latter in Fig. 9 for different μ_α and μ_β . While the dashed line corresponds to the fit providing A , we see again a scattering of the simulations results, with a small enough amplitude that validates the scaling $V \sim \rho$. In opposition to the case $c_\infty = 0$, i.e., $\eta = 0.5$, the α/β interface is vertical only when $\mu_\alpha = \mu_\beta = 0$. This is indeed the usual assumption when one studies eutectic growth within the one-sided model at an arbitrary global composition [24]. However, as soon as the diffusion coefficient in the growing phases is finite, the α/β interface becomes curved. Noticeably, when $\mu_\alpha = \mu_\beta$, the width of the lamella with the larger (smaller) phase fraction, here β (α), is larger (smaller) at the triple junction than at equilibrium,

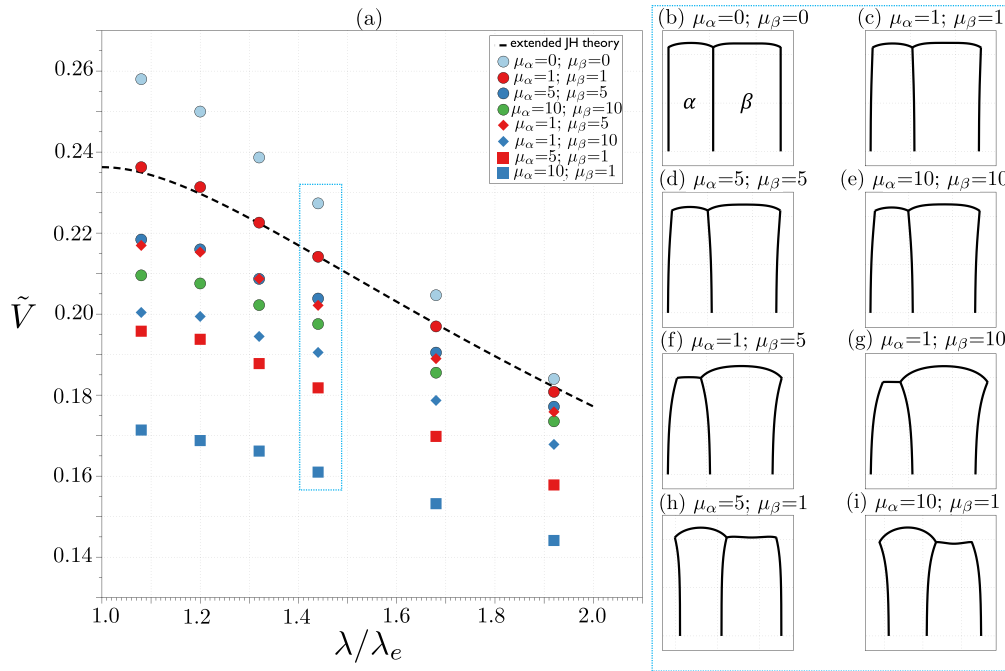


FIG. 9. (a) Rescaled dimensionless growth velocities obtained from NPF simulations at an off-eutectoid composition for different μ_α and μ_β . (b)–(i) show the alteration of the lamellar shapes extracted from NPF simulations for $\lambda/\lambda_e = 1.44$.

i.e., far behind the triple junction. This yields a rotation of the triple junction. This rotation is further accentuated when $\mu_\beta > \mu_\alpha$, and in opposition, when $\mu_\beta < \mu_\alpha$, the sign of the rotation angle is opposite.

Until now it was proposed that the scatter observed for \tilde{V} in our results, i.e., in Figs. 5, 8, and 9, is due to the inaccuracy of the theory developed in Ref. [6]. However, it should be verified that this scatter is not instead related to interfacial effects, that are eliminated with different choices of parameters when μ_α and μ_β change. Therefore, here, we finally perform a convergence study with respect to \tilde{d}/W . For the sake of generality, we choose the asymmetric situation where

$c_\infty = 0$, $\mu_\alpha = 10$, and $\mu_\beta = 3$. This corresponds to a result presented in Fig. 8, more precisely the third blue diamond when starting from the left. In Fig. 10, we present the convergence of \tilde{V} when \tilde{d}/W increases, i.e., when the interface width W decreases. At the interface width used in Fig. 8 (and also in Figs. 5 and 9), i.e., for the encircled data point at $\tilde{d}/W = 0.5$, a 2% error on \tilde{V} is found (compared to the converged value), which is quite satisfactory. This supports that the scatter observed in our results is indeed due to the, small but still existing, inaccuracy of the theory developed in Ref. [6].

V. CONCLUSIONS

In this paper, we have developed a quantitative nondiagonal phase field model for three-phase transformations, such as eutectic and eutectoid. In the latter case, the diffusion coefficients in the growing phases D_α and D_β are of the same order as the diffusion coefficient in the mother phase D_γ , and a kinetic cross coupling between the diffusion field and the phase fields is thus required. Special attention is paid to the elimination of all abnormal interface effects that arise when analyzing the thin-interface limit of the model.

First, we have benchmarked our model against phase field and boundary integral results from Ref. [11] in the one-sided case (when $D_\alpha = D_\beta = 0$). Second, we have performed simulations in the two-sided case where D_α and D_β are non-negligible. We evidence the relevance of the scaling law suggested in Ref. [6] for the steady-state velocity as a function of the ratio of diffusion coefficients. We observe the two limiting cases, i.e., the classical one for which diffusion is mainly present in the mother phase due to $D_\alpha, D_\beta \ll D_\gamma$, and the one for which diffusion is mainly present in the growing

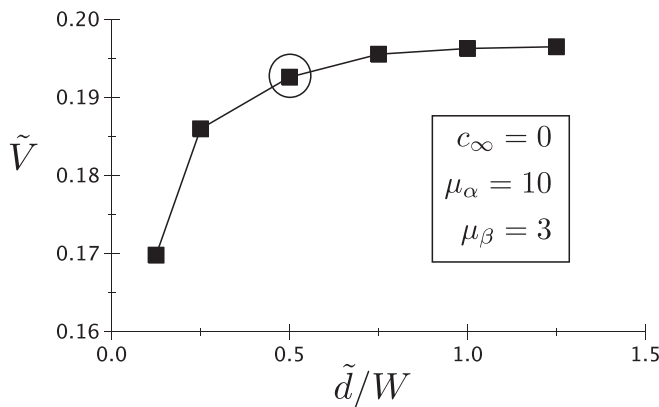


FIG. 10. Convergence study with the interface width W for a situation corresponding to Fig. 8, i.e., $c_\infty = 0$, $\mu_\alpha = 10$, $\mu_\beta = 3$. The encircled data point for $\tilde{d}/W = 0.5$, that corresponds to the interface width used in Fig. 8 (and also in Figs. 5 and 9), shows a 2% error compared to the converged value of \tilde{V} , which is quite satisfactory.

phases due to $D_\alpha, D_\beta \gg D_\gamma$. In both one- and two-sided cases we verify the necessity of using a nondiagonal phase field model, i.e., having a kinetic cross coupling, for quantitative simulations.

In the present work, the influence of the bulk diffusion in the growing phase has been investigated. During eutectoid transformations such as the pearlite transformation, not only bulk diffusion in the growing ferrite but also surface diffusion are believed to play a crucial role. The nondiagonal phase field model provides the possibility to tune the surface diffusion coefficient, while eliminating other kinetic effects such as solute trapping. Thus, it may be a potential tool for a future study of the pearlite transformation at a steady state and the divorced pearlite microstructure [25,26] with the consideration of all possible diffusion paths. In this regard, the complex thermodynamics of pearlite may necessitate

the usage of a phase field model based on a grand-potential formulation [27].

ACKNOWLEDGMENTS

This work is supported by the China Scholarship Council (CSC) Grant No. 201706370221 and we thank the BMBF for funding via the program Meet HiEnd III. One of the authors (G.B.) acknowledges the financial support provided by the Deutsche Forschungsgemeinschaft (DFG) in the framework of the Priority Program SPP2122 under Grant No. 409726740. The authors gratefully acknowledge the computing time granted by the JARA Vergabegremium and provided on the JARA Partition part of the supercomputer JURECA at Forschungszentrum Jülich [28].

-
- [1] C. De Rosa, C. Park, and E. Thomas, *Nature (London)* **405**, 433 (2000).
 - [2] T. Oyama, O. D. Sherby, J. Wadsworth, and B. Walser, *Scr. Metall.* **18**, 799 (1984).
 - [3] C. Zener, *Trans. AIME* **167**, 550 (1947).
 - [4] M. Hillert, *Jernkontorets Ann.* **141**, 757 (1957).
 - [5] J. Hunt and K. Jackson, *Trans. Metall. Soc. AIME* **236**, 843 (1966).
 - [6] K. Ankit, A. Choudhury, C. Qin, S. Schulz, M. McDaniel, and B. Nestler, *Acta Mater.* **61**, 4245 (2013).
 - [7] A. Karma, *Phys. Rev. E* **49**, 2245 (1994).
 - [8] S. G. Kim, W. T. Kim, T. Suzuki, and M. Ode, *J. Cryst. Growth* **261**, 135 (2004).
 - [9] B. Nestler and A. A. Wheeler, *Physica D* **138**, 114 (2000).
 - [10] A. A. Wheeler, G. B. McFadden, and W. J. Boettinger, *Proc. R. Soc. London, Ser. A* **452**, 495 (1996).
 - [11] R. Folch and M. Plapp, *Phys. Rev. E* **72**, 011602 (2005).
 - [12] A. Karma and W. J. Rappel, *Phys. Rev. E* **57**, 4323 (1998).
 - [13] A. Karma, *Phys. Rev. Lett.* **87**, 115701 (2001).
 - [14] R. F. Almgren, *SIAM J. Appl. Math.* **59**, 2086 (1999).
 - [15] E. A. Brener and G. Boussinot, *Phys. Rev. E* **86**, 060601(R) (2012).
 - [16] G. Boussinot and E. A. Brener, *Phys. Rev. E* **89**, 060402(R) (2014).
 - [17] G. Boussinot and E. A. Brener, *Phys. Rev. E* **88**, 022406 (2013).
 - [18] G. Boussinot, E. A. Brener, C. Hüter, and R. Spatschek, *Continuum Mech. Thermodyn.* **29**, 969 (2017).
 - [19] K. Wang, G. Boussinot, C. Hüter, E. A. Brener, and R. Spatschek, *Phys. Rev. Mater.* **4**, 033802 (2020).
 - [20] M. Ohno and K. Matsuura, *Acta Mater.* **58**, 5749 (2010).
 - [21] M. Ohno and K. Matsuura, *Acta Mater.* **58**, 6134 (2010).
 - [22] M. Nicoli, M. Plapp, and H. Henry, *Phys. Rev. E* **84**, 046707 (2011).
 - [23] M. Ohno, T. Takaki, and Y. Shibuta, *Phys. Rev. E* **96**, 033311 (2017).
 - [24] K. Kassner and C. Misbah, *Phys. Rev. A* **44**, 6513 (1991).
 - [25] J. D. Verhoeven and E. D. Gibson, *Metall. Mater. Trans. A* **29**, 1181 (1998).
 - [26] K. Ankit, R. Mukherjee, T. Mittnacht, and B. Nestler, *Acta Mater.* **81**, 204 (2014).
 - [27] M. Plapp, *Phys. Rev. E* **84**, 031601 (2011).
 - [28] Jülich Supercomputing Centre, JURECA: Modular supercomputer at Jülich Supercomputing Centre, *J. Large-Scale Res. Facil.* **4**, A132 (2018).